ELECTRONIC SUPPLEMENTARY INFORMATION FOR

Ozone uptake by commercial brake pads and brake pad components: assessing the potential indirect air quality impacts of non-exhaust emissions

Laura C. Matchett,[1,2] Maya Abou-Ghanem,[2]
Kristyna A. R. Stix,[2] Devon T. McGrath,[3] Sarah A. Styler [1,2]*

*Corresponding author; email: stylers@mcmaster.ca

[1] Department of Chemistry & Chemical Biology, McMaster University, Hamilton, Canada, L8S 4L8
[2] Department of Chemistry, University of Alberta, Edmonton, Alberta, Canada, T6G 2G2
[3] Department of Chemistry, Memorial University of Newfoundland, St. John's, Newfoundland and Labrador, Canada, A1C 5S7

Number of pages: 37
Number of figures: 3
Number of tables: 11

1 Materials and methods

1 Materials and methods

1.1 Photochemical coated-wall flow tube reactor

The coated-wall flow tube consists of a water-jacketed Pyrex tube into which a sample-coated Pyrex insert tube (20.0 cm length, 1.5 cm id) can be placed. The flow tube is surrounded by four UV-A lamps (300–410 nm, λ_{max}: 356 nm), which give a NO_2 photolysis frequency (J_{NO_2}) of 0.0045 ± 0.0001 s^{-1}.[1] Although this value is within the range of reported ground-level values,[2,3] our lamp spectrum differs from the solar radiation spectrum; consequently, the absolute comparisons between samples reported here may differ from those made under ambient conditions.

Experiments were conducted in a flow of purified air (provided by a commercial zero air generator; 747-30 reactor type A, Aadco Instruments), which was directed to three mass flow controllers (MFC; Alicat). The first MFC, which controlled the supply of zero air to a commercial UV ozone generator (97-0066-01, UVP), was set to 50 sccm. The second and third MFCs controlled the flows of dry air and wet air, the latter obtained by passing dry air through a water bubbler, with the ratio of the flows determining the relative humidity (RH); the total flow was always set to 350 sccm. The output of the three MFCs was mixed and introduced to the flow tube using a movable injector. At these flow rates and for our flow tube dimensions, laminar flow was reached within 2.2 cm (*i.e.*, prior to the sample coating). Ozone mixing ratios were measured using a photometric ozone analyzer (T400, Teledyne); to meet the flow requirements of the analyzer (~700 sccm), the outflow of the reactor was mixed with a make-up dry air flow (500 sccm) upstream of the analyzer inlet. All reported

ozone mixing ratios were corrected for this dilution. Additional details regarding this experimental system are presented in Abou-Ghanem et al.[1]

1.2 Grinding of brake pads

At the beginning of the study, brake pads were broken up into small pieces using a hammer; then, prior to each experiment, appropriately sized pieces were ground into a fine powder using a Wig-L-Bug (multi speed digital, Dentsply Rinn) grinder mixer (30 s, 3800 rpm) equipped with a stainless steel vial (1.3 cm id, 2.5 cm length; 3.3 cm^3 volume) and a single stainless steel ball pestle (0.6 cm diameter). All grinding was conducted in a fume hood to prevent inhalation of particles. The size distribution of our particles may differ from that of "real-world" brake wear, which is why we normalized our uptake coefficients to specific surface are (see Section 1.7). Additionally, we believe that the potential compositional differences described in the main text, and not the size distribution differences, will be the driving force for any reactivity differences between our samples and "real-world" brake wear.

1.3 Brake pad component chemical information

The following brake pad components were used as received: phenolic resin (powder, cured; Hexion), graphite (powder, synthetic, <20 μm; Sigma Aldrich), Fe (powder, 99+% metal basis, <74 μm; Alfa Aesar), Fe_2O_3 (powder, ≥ 96%, <5 μm; Sigma Aldrich), Fe_3O_4 (powder, 95%, <5 μm; Sigma Aldrich), and Cu (powder, 99.9% metal basis, 37–88 μm; Alfa Aesar).

1.4 Preparation of sample-coated Pyrex insert tubes

1.4.1 Cleaning

Pyrex insert tubes were cleaned before each use by placing them in a 1% acid bath for 1 min, rinsing with deionized water, placing them in a concentrated base bath for 1 h, and rinsing again with deionized water. After cleaning, tubes were dried in a gravity oven (100 L, Fisherbrand). Chemical-resistant gloves and tongs were used when handling the tubes from the acid and base baths. The acid bath was prepared by diluting 10 mL of concentrated H_2SO_4 (reagent grade, Caledon Laboratory Chemicals) in 990 mL of deionized water. The base bath was prepared by dissolving 41.7 g of KOH pellets (ACS reagent ≥ 85%, Sigma Aldrich) in a solution of 1 L of 2-propanol (certified ACS plus, Fisher Chemicals) and 166 mL of deionized water. Deionized water (18 MΩ) was obtained from a Millipore Synergy UV ultrapure water system.

1.4.2 Coating

Pyrex insert tubes were coated the day before experiments were performed. As all samples were highly reactive toward ozone, obtaining reasonable diffusion corrections (see **Section S1.8**) required the use of very small sample masses. To aid in tube coating, therefore, we mixed all samples with SiO_2, which has a very low reactivity with ozone (**Fig. S1**).

For each experiment, known quantities of sample (brake pad or brake pad component) and SiO_2 (amorphous powder, 99.0% trace metal basis; Alfa Aesar) were mixed with a minimal quantity of deionized water in a clean stoppered tube. The tube was shaken to disperse the mixture and subsequently rotated on a heated hot dog roller (RHD800 Retro Series Hot Dog

190 Roller, Nostalgia Electrics) until dry. To ensure the incoming gas stream reached laminar flow prior to the coating and to remove areas of uneven coating distribution, moistened laboratory wipes (Kimberly-Clark S9 Professional™) were used to remove coating from both ends of the tube and obtain a final coated length of 14 cm. All tubes were placed in a gravity oven overnight prior to use.

1.5 Experimental protocol

At the beginning of each experiment, the movable injector was retracted such that the sample-coated tube was exposed to zero air at 25% RH for 15 min. The injector was then pushed past the coated tube and the ozone generator was turned on to measure the ozone mixing ratio in the gas stream entering the flow tube (*i.e.*, in the absence of exposure to the sample). Once the ozone mixing ratio was stable (30 min), the injector was pulled back and the tube was exposed to ozone for a total of 3 h 30 min (2 h dark, 1 h light, 30 min dark); after sample exposure, to account for any drift in signal, the injector was pushed past the coated tube and the ozone mixing ratio was again measured for 30 min. Finally, the ozone generator was turned off and data were collected for a further 5 min. This sequence is displayed graphically in **Figs. S1** and **S2**.

1.6 Determination of sample mass

Total coating masses (*i.e.*, brake pad/component + SiO_2) were determined by difference. In particular, following ozone exposure (as described in **Section S1.5**), coated Pyrex insert tubes were weighed in triplicate, cleaned, and then re-weighed in triplicate using an analytical balance (AB265-S/FACT, Mettler Toledo). The respective masses of brake

pad/component and SiO_2 were determined by assuming that their ratio remained constant during the coating process. The cleaning procedure consisted of using a test tube brush and a water/Sparkleen™ (Fisherbrand™) mixture to remove the coating, followed by rinsing with distilled water, then with methanol (Optima grade, Fisher Chemicals), and finally with deionized water. The tubes were then dried in a gravity oven prior to re-weighing.

1.7 Data analysis

We quantified sample reactivity using a parameter known as an uptake coefficient (γ), which represents the fraction of ozone–surface collisions that leads to ozone loss from the gas phase.[4] In the following discussion, "sample" refers to brake pad or brake pad component and "total" refers to the mixture of the sample and SiO_2.

First, the pseudo-first-order rate constant for ozone loss, $k_{obs,total}$, was calculated for the sample–SiO_2 mixture as follows:[5]

$$[O_3] = [O_3]_0 \times e^{-k_{obs,\,total} \times t} \quad \text{(S1)}$$

Here, $[O_3]$ is the average ozone mixing ratio (ppb) when the sample was exposed to ozone, $[O_3]_0$ is the average ozone mixing ratio (ppb) without sample exposure, and t is the residence time of ozone inside the coated section of the tube (s). For the steady-state uptake coefficients ($\gamma_{BET,SS}$), $[O_3]$ was determined by averaging the last 5 min of data for the light or second dark periods. For the time-dependent uptake coefficients ($\gamma_{BET,15min}$, $\gamma_{BET,30min}$, and $\gamma_{BET,60min}$), $[O_3]$ was determined by averaging the data over 3 min intervals at the time of interest (15, 30, or 60 min after ozone exposure was initiated in the dark).

Since the SiO_2 matrix exhibited non-negligible photochemistry under our conditions (**Fig. S1**), we corrected for its contribution to the pseudo-first-order rate constants obtained using our experimental data. To do this, we performed triplicate experiments with 10 mg of SiO_2 and applied **Eqs. S1** and **S3–S5** to determine an average $\gamma_{BET,\,SiO_2}$(here, the subscript "sample" refers to SiO_2). Then, by rearranging **Eqs. S3–S5**, we used this value to back-calculate $\gamma_{eff,\,SiO_2}$ and $k_{obs,\,SiO_2}$ values appropriate for the specific mass of SiO_2 in each sample–SiO_2 mixture. Finally, we determined the pseudo-first-order rate constant for the sample alone, $k_{\text{obs,sample}}$, by subtraction:

$$k_{obs,\,sample} = k_{obs,total} - k_{obs,SiO_2} \qquad \text{(S2)}$$

Using $k_{\text{obs,sample}}$, we calculated the effective uptake coefficient, $\gamma_{\text{eff,sample}}$, as follows:[5]

$$\gamma_{eff,\,sample} = \frac{D_{tube} \times k_{obs,sample}}{\omega_{O_3}} \qquad \text{(S3)}$$

Here, D_{tube} is the diameter of the flow tube (m) and ω_{O_3} is the mean thermal velocity of ozone under our experimental conditions (m s^{-1}).[1]

Under our conditions of both laminar (Reynolds number < 2000) and continuum (Knudsen number << 1) flow,[1] limitations in the radial diffusion of ozone from the center of the tube can result in depletion of near-surface ozone mixing ratios at high values of γ_{eff}. This depletion results in a lower total ozone loss to the surface of the coating, and correspondingly

to underestimations of γ_{eff}. We corrected for this effect using the Knopf–Pöschl–Shiraiwa (KPS) method:[6]

$$\gamma_{corr,\,sample} = \frac{\gamma_{eff,sample}}{1 \; - \; \gamma_{eff,total} \dfrac{3}{2N_{shw}^{eff} \times \; Kn}} \qquad \text{(S4)}$$

Here, N_{shw}^{eff} is the effective Sherwood number and *Kn* is the Knudsen number. The correction factor (denominator) uses $\gamma_{eff,total}$ (*i.e.*, sample–SiO_2 mixture) rather than $\gamma_{eff,sample}$ because diffusion limitations arise from the overall reactivity of the coating, rather than the reactivity of its individual components. In this study, we chose sample masses such that the diffusion correction factors never exceeded 15% at steady state. However, in the case of the time-dependent uptake coefficients, some correction factors did exceed 15% due to the large initial sample reactivities; all correction factors are shown in **Table S10**. For the brake pads, the correction factors at 15 min were very large, changing the uptake coefficients by up to an order of magnitude; as a result, we do not report $\gamma_{BET,15min}$ values.

Finally, we scaled $\gamma_{corr,sample}$ using the specific surface area (Brunauer–Emmett–Teller; BET) to obtain γ_{BET}, the values reported in this work:

$$\gamma_{BET,sample} = \gamma_{corr,sample} \times \frac{S_{geo}}{S_{BET,\,sample} \times \; m_{sample}} \qquad \text{(S5)}$$

Here, S_{geo} is the geometric surface area of the coated portion of the tube (m^2), $S_{BET,\,sample}$ is the specific surface area of the sample ($m^2\ g^{-1}$), and m_{sample} is the mass of the sample (g).

1.8 Reasoning for using an SiO_2 matrix and selection of the sample to SiO_2 ratio

As described in **Section S1.7**, the ability to quantify trace gas–surface reaction kinetics for highly reactive samples using atmospheric pressure coated-wall flow tubes can be limited by diffusion of ozone to the sample surface. Although we can correct for this effect (**Eq. S4**), the high reactivity of the brake pad samples studied here necessitated large diffusion corrections (up to 40% under illuminated conditions), even at sample masses much lower than those typically used in flow tube studies.[1,7,8] To facilitate the use of small brake pad quantities (< 3 mg), while still obtaining uniform and reproducible tube coatings, we prepared samples as mixtures with SiO_2, as has been previously reported for similarly reactive mineral dust proxies.[1,8]

To ensure that the sample reactivity could be distinguished from the SiO_2 reactivity after subtraction, we chose amounts of sample and SiO_2 such that k_{obs,SiO_2} accounted for less than 20% of $k_{obs,total}$. For the organic PBR, ceramic NAPA, and semi-metallic NAPA samples, this condition was met with a sample–SiO_2 mixture consisting of 15% sample and 85% SiO_2 (by mass). Smaller decreases in ozone were observed for the ceramic and semi-metallic PBR samples, so a mixture consisting of 25% sample was used. For consistency, we used mixtures containing 35% sample for all brake pad component experiments. A total (sample + SiO_2) mass of 10 mg was used for all experiments; all sample and SiO_2 masses used are presented in **Table S2**.

1.9 Specific surface area (Brunauer–Emmett–Teller; BET) determination by nitrogen adsorption analysis

Surface area determinations were conducted using nitrogen adsorption analysis (3Flex, Micromeritics), as described in Abou-Ghanem et al.[1] Sample degassing was performed at room temperature, rather than at elevated temperatures, as this avoided removal of strongly surface-sorbed water, which we expect to be present under our coated-wall flow tube experimental conditions. The Brunauer–Emmett–Teller (BET) nitrogen-accessible surface area was determined by fitting the linear BET equation and ensuring the 4-point criterion was met.[9] The specific surface areas for all samples are presented in **Table S3**.

1.10 Determination of uptake coefficient errors

The overall experimental uncertainty associated with each reported uptake coefficient was obtained by propagating the random errors associated with each variable in the calculations described in **Section S1.7**. The errors associated with the sample mass, ozone mixing ratios, and k_{obs,SiO_2}were the standard deviations of the triplicate weighing of the tubes, the ozone mixing ratios over the relevant averaging period, and the triplicate SiO_2-only experiments, respectively. The contribution from the uncertainty in the MFC readings was negligible (<1%), so was not included here. The errors associated with the specific BET surface areas were determined by adding or subtracting points from both the low- and high-pressure ends of the adsorption isotherms' acceptable BET range. These 1- and 2-point deviations, in both the low- and high-pressure ranges, gave slightly different BET surface area values than those reported in **Table S3**; we used these values to determine an approximate standard deviation for each measurement. The BET surface area values reported abide by the 4-point BET criterion and possess an R^2 value as close to 1 as possible.[9]

1.11 Brake pad characterization

1.11.1 Elemental analysis by inductively coupled plasma mass spectrometry (ICP-MS)

Brake pad elemental composition was determined using inductively coupled plasma mass spectrometry (ICP-MS, 58 elements; Perkin Elmer Elan 6000); the results of these analyses are presented in **Fig. 2** and **Table S4**. Samples were digested in a 10:1 mixture of HF:HNO_3 and heated on a hot plate held at 110°C until dry. Then, 8M HNO_3 was added and the mixture was again evaporated until dry. Finally, the residue was dissolved in 2% HNO_3 for analysis. A 4-point external calibration with blank was performed using a standard element mixture prior to sample analysis. To account for any instrument signal drift, sample digests were spiked with 10 ppb of Sc, In, and Bi as internal standards.

1.11.2 Total carbon and nitrogen by combustion analysis

Brake pad total C and total N were determined by dry combustion analysis (Flash 2000 Organic Elemental Analyzer, Thermo Fisher). A known mass of each sample was placed into the combustion tube with chromium oxide and cobaltous oxide silver catalysts. Purified oxygen was introduced to the tube to generate a flash combustion reaction with a maximum temperature of 1800–2000°C, which converted the carbon and nitrogen in the samples to CO_2 and NO_x gas, respectively. NO_x is subsequently reduced to N_2 by copper wires in a reduction furnace. The CO_2 and N_2 combustion gases were separated on a packed chromatographic column (Porapak QS 80/100 mesh) and detected using a thermal conductivity detector. Acetanilide was used as a calibration standard and a birch leaf

certified standard (certificate no. 136621) was used as an external reference standard for both carbon and nitrogen. These results are presented in **Fig. 2** and **Table S4**.

1.11.3 Organic and elemental carbon by thermogravimetric analysis (TGA)

Brake pad organic carbon (*e.g.,* phenolic resin) and elemental carbon (*e.g.,* graphite) were determined using TGA (Mettler Toledo TGA/DSC 1 STARe System with SDTA sensor). The sample (~10 mg) was heated in an alumina crucible from 25°C to 950°C at a rate of 10°C min^{-1} in a flow of air. The TGA curves are shown in **Fig. S3**.

1.11.4 Crystalline phase identification by X-ray diffraction analysis

X-ray diffraction (XRD) patterns of the ground brake pads were collected using a Bruker D8 DISCOVER with DAVINCI.DESIGN diffractometer equipped with a Co sealed tube radiation source (λ_{avg} = 1.79026 Å) operated at 35 kV and 45 mA. The 2D frames were collected with DIFFRAC.Measurement Centre Version 7.5 software and integrated to 1D frames using DIFFRAC.EVA Version 5.1 software. Phase searching was performed using the integrated ICDD PDF-4+ 2020 powder database in DIFFRAC.EVA. All software packages are from Bruker-AXS. Crystalline phases identified are presented in **Table S5**.

2 Sample characterization discussion

2.1 Phases identified by XRD

The crystalline phases identified by XRD and shown in **Table S5** are separated into two categories: good matches and potential matches. “Good” matches indicate phases for which peaks were well resolved and multiple peaks lined up with the database, thereby giving

confidence to the phase identification. “Potential” matches indicate phases where only several peaks matched with the database, or where the matching peaks had low resolution because of weak peak signals and/or high background noise. Thus, it is possible that some of the “potential” phases are not present in the samples (specific examples are discussed below). In addition, due to the complexity of our samples and resulting XRD patterns, not all elements detected by ICP-MS are accounted for in the XRD components identified; for example, in the case of the organic PBR sample, Mg, Al, K, Ca, and Sb were detected by ICP-MS, but not accounted for in the identified phases. Thus, additional components may be present in the samples, despite not being identified by XRD; a list of components identified in brake pads in the published literature is shown in **Table S7**.

For the NAPA samples, our XRD results generally agree with the compositional information provided in the manufacturer’s safety data sheets (SDS, **Table S6**). For the PBR samples, no SDS were provided; however, we can still comment on the XRD results. Compared to the other PBR samples, the ceramic PBR has the longest list of phases identified, which is consistent with it having a higher elemental diversity (from ICP-MS), and contains more ceramic fibers, metal sulfides, and metal oxides. However, it is probable that some of these potential matches are not present. Specifically, some of the potential phases identified contained elements found in <0.1 wt.% by ICP-MS: Co (0.003%), Ni (0.01%), Li (<0.001%), and Sn (0.003%). From this list, Co is the only element that was also present in a compound with a “good” phase match (zinc cobalt sulfide), and since its stoichiometry in this compound is small, its presence in the ceramic PBR sample is a stronger possibility. In contrast, the semi-metallic and organic PBR samples had much smaller lists of phases identified, which is

consistent with the fact that a smaller number of elements was detected for these samples by ICP-MS.

2.2 Mass fraction unaccounted for by ICP-MS and combustion analysis

In most cases, the elemental composition quantified by ICP-MS and combustion analysis does not account for 100% of brake pad sample mass (**Table S4**). This discrepancy likely reflects contributions from O, S, Si, and Zr, none of which were measured here. O, in the form of organics, metal oxides, and ceramic fibers, can make up 20–35% of brake pads.[10,11] S, in the form of metal sulfides and/or sulfates, has been found to comprise 2–8% of brake pads.[10,12–14] Si and Zr, in the form of ceramic fibers (*e.g.*, zircon ($ZrSiO_4$) and quartz (SiO_4)) or clays,[12,15] have been found to comprise up to 15% [10,13,14,16] and 25% [10,13] of brake pads, respectively. Another potential contributor to the discrepancy is the underestimation of Al, as its ICP-MS recovery was 64%.

For both NAPA samples, ICP-MS and combustion analysis quantified ~45% of the samples. Based on the composition from the SDS (**Table S6**) and phases identified by XRD (**Table S5**), we know that O, S, and Si are present in multiple components in both samples and Zr is potentially present in the semi-metallic sample. Based on the typical content of these elements in brake pads highlighted in the previous paragraph, we can hypothesize that the quantification of O, S, Si, and Zr would fully account for the "missing" mass of the NAPA samples.

Although the results from ICP-MS and combustion analysis appear to account for 100% of the mass of the semi-metallic PBR sample, the XRD phases identified also contain O and S,

and potentially contain Si and Zr. A possible explanation for this discrepancy is that the ICP-MS recovery for Fe was 122%, which could have led to a significant overestimation of the Fe content for this (mostly Fe) sample. The ceramic PBR sample, which was 73% quantified, also had many phases containing O, with some also containing S, Si, and Zr. As the inclusion of these phases would more than account for the "missing" mass of this sample, we conclude that its Fe content may also be overestimated. The organic sample had the lowest quantification (36%) by ICP-MS and combustion analysis. Although the XRD phases identified do contain O, S, and Si, they are likely insufficient to bring the quantification to 100%; instead, we suggest that the sample likely contains additional components that contain these elements (or Zr, potentially).

2.3 Organic and elemental carbon content by TGA

We used TGA to quantify the organic and elemental carbon content of the brake pads; the results of these analyses are shown in **Fig. S3**. For the ceramic and organic PBR samples, two distinct mass losses can be identified: the first, from approximately 250°C to 600°C, corresponds to oxidative thermal degradation of organic species (*e.g.*, phenolic resin, aramid fibers, cashew resin); the second, from approximately 600°C to 800°C, corresponds to the oxidative degradation of elemental carbon species (graphite or carbon black).[17] The two NAPA samples do not have as distinct a plateau between the two regions, so the inflection point was used to separate the mass losses.

The Fe-rich semi-metallic and ceramic PBR samples both display visible interference from Fe oxidation (400–900°C)[18], which has previously been reported for brake pads.[12,18] Specifically, in the case of the semi-metallic PBR sample, the expected mass losses are

obscured by an increase in mass starting at 500°C, which precludes us from drawing conclusions regarding the organic and elemental carbon content of this sample. In the case of the ceramic PBR sample, a small increase in mass is visible at ~800°C; since Fe oxidation typically begins at ~400°C and overlaps with the temperature ranges of both organic and elemental carbon degradation, this result indicates that we are likely underestimating the sample's elemental carbon content and perhaps underestimating its organic carbon content. This inference is supported by the fact that the total TGA mass loss (17%) for this sample is lower than the total carbon content obtained by combustion analysis (22%).

The TGA curves (**Fig. S3**) shows that all samples have a similar organic content (within 2%), and thus likely contain a similar amount of phenolic resin binder. In general, the NAPA samples contain more elemental carbon than the PBR samples. This elemental carbon is most likely present as graphite, which is typically used as a lubricant.[15] In the case of the PBR samples, it appears that some of the graphite may have been replaced by metal sulfides, another lubricant class,[15] as these samples contain more Cu, Sn, and Sb than the NAPA samples.

3 Ozone flux calculations and discussion

To assess the potential impact of brake wear on urban ozone concentrations, we compared the flux of ozone to the surface of brake wear PM with its flux to the surface of the ground using a method similar to that described by Li et al.[19] The flux of ozone to the ground (F_{grd} , mol m^{-2} s^{-1}) can be calculated using the following equation:

$$F_{grd} = - V_d \times [X_g] \times 10^{-2} \quad \text{(S6)}$$

Here, V_d is the deposition velocity of the ozone (cm s^{-1}), and $[X_g]$ is the ozone concentration (mol m^{-3}).

The flux of ozone to brake wear PM (F_{PM}, mol m^{-2} s^{-1}), can be calculated as:

$$F_{PM} = \frac{\gamma_{eff} \times \omega}{4} A \times h \times [X_g] \times 10^{-6} \quad \text{(S7)}$$

Here, γ_{eff} is the effective uptake coefficient (15 min, 30 min, 60 min, or steady-state), ω is the mean thermal velocity of the gas (m s^{-1}), A is the PM surface area density (μm^2 cm^{-3}), h is the mixing height (m), and $[X_g]$ is the ozone concentration (mol m^{-3}).

We used values of 0.15 cm s^{-1} for V_d,[19] 300 m for h, and 359.4 m s^{-1} for ω.[1] Studies in Toronto and Barcelona found brake wear $PM_{2.5}$ loadings of 1.5 μg m^{-3} and 1.2 μg m^{-3}, respectively;[20,21] using the average of these values, and assuming a particle diameter of 1 μm and a density of 2.6 g cm^{-3},[13] we estimated the PM surface density (A) of brake wear to be 3.12 μm^2 cm^{-3}.

To calculate the percentage of the ground loss these loadings represent, we used the time-dependent and steady-state γ_{BET} values determined in this study. We found that in all cases the loss of ozone to the particles is < 1% of the loss of ozone to the ground. Although PM_{10} loadings of brake wear are typically larger (*e.g.*, 4.2 μg m^{-3} in Barcelona)[21], this would not result in an increase in F_{PM} because of the smaller surface-to-volume (*i.e.*, mass) ratio of these larger particles. Thus, we conclude that brake wear will have a minimal effect on ozone concentrations.

We also assessed how ozone loss to brake wear compares to loss to organic near-road PM.[20] In the aerosol flux equation (**Eq. S7**), the only parameters that are aerosol type-dependent

are the uptake coefficient and the surface area density; thus, we can compare the product of these two values to determine the relative importance of ozone loss to different PM types. To do so, we used data from a study conducted in Toronto, Canada in 2016,[20] which reported both brake wear and organic PM mass loadings. Specifically, we used the data from this study's highway site during morning rush hour (1.5 μg m^{-3} for brake wear and 7 μg m^{-3} for organic PM), which represented the highest brake wear loadings.[20] We converted these values to aerosol surface density by assuming a particle diameter of 1 μm,[22,23] a brake wear density of 2.6 g cm^{-3},[13] and an organic PM density of 1.3 g cm^{-3}.[24] To select an uptake coefficient for the organic PM, we needed to understand its composition. The Toronto study determined that the organics consisted of a highly oxygenated and aged fraction (40%), a freshly formed secondary organic aerosol fraction (10%), and a traffic-related hydrocarbon-like fraction (50%).[20] Using studies on exhaust emissions, the traffic-related fraction can be further divided into alkanes (~75%) and species containing double bonds or other functional groups (*e.g.*, aldehydes, ketones, acids) (~25%).[25,26] We assume that the alkanes are non-reactive with ozone and, to simplify our analysis, use a single uptake coefficient for the remaining reactive fraction. We choose a value of 4×10^{-6}, which is representative of humic acid in the dark, because humic-like substances comprise part of the organic fraction of multiple different PM types.[27] Although the reactivity of ozone with compounds containing double bonds is higher (*e.g.,* ~10^{-4} for oleic acid[28] and alkenes[29]), we expect the alkene subfraction of the reactive organic PM fraction to have experienced some degree of aging, which would decrease its reactivity toward further oxidation.

Using the information outlined above and the various uptake coefficients determined in this study, we identified cases in which brake wear would likely be a more important ozone sink

than organic PM. Using the steady-state values for ozone uptake by brake wear ($\gamma_{BET,SS}$), organic PM dominates ozone loss; however, if we use $\gamma_{BET,30min}$, which is more realistic for fresh brake wear emissions during rush hour periods, brake wear dominates ozone loss for the ceramic and organic PBR brake pads. Specifically, the calculated fluxes of ozone to ceramic and organic PBR samples are 4 and 1.5 times larger than the calculated flux to organic PM, respectively. Additionally, although high diffusion correction factors prevented us from reporting reliable $\gamma_{BET,15min}$ values for the brake pads, these values are larger than $\gamma_{BET,30min}$ in all cases; over this timescale, uptake of ozone by all brake pad samples is larger than by organic PM.

Here, we focused our analysis on dark ozone uptake as we were mainly interested in comparisons to our larger time-dependent uptake coefficients, which we could only determine under dark conditions for our experiments. However, as both humic acid and our brake pads display photoenhanced ozone uptake, the flux comparison may be different under light conditions. The ozone uptake coefficient is approximately one order of magnitude larger in the light than in the dark for humic acid,[27] but only a factor of 2–3 larger for brake pads (**Fig. 3a**). Thus, in the daytime, ozone flux to organic PM will likely increase more than ozone flux to brake wear. However, we still predict that, for our more reactive samples (ceramic and organic PBR), daytime ozone loss to brake wear will be comparable to ozone loss to organic PM. Morning rush hour also occurs before sunrise for many months in the winter, during which time our dark analysis would be applicable.

4 Supporting figures

Fig. S1 Representative reaction profiles for the five brake pads and SiO_2. The blue and yellow underlays indicate periods of exposure to ozone in the dark and light, respectively. The black line is smoothed data (3 min moving average) and the pink line is the original unsmoothed data.

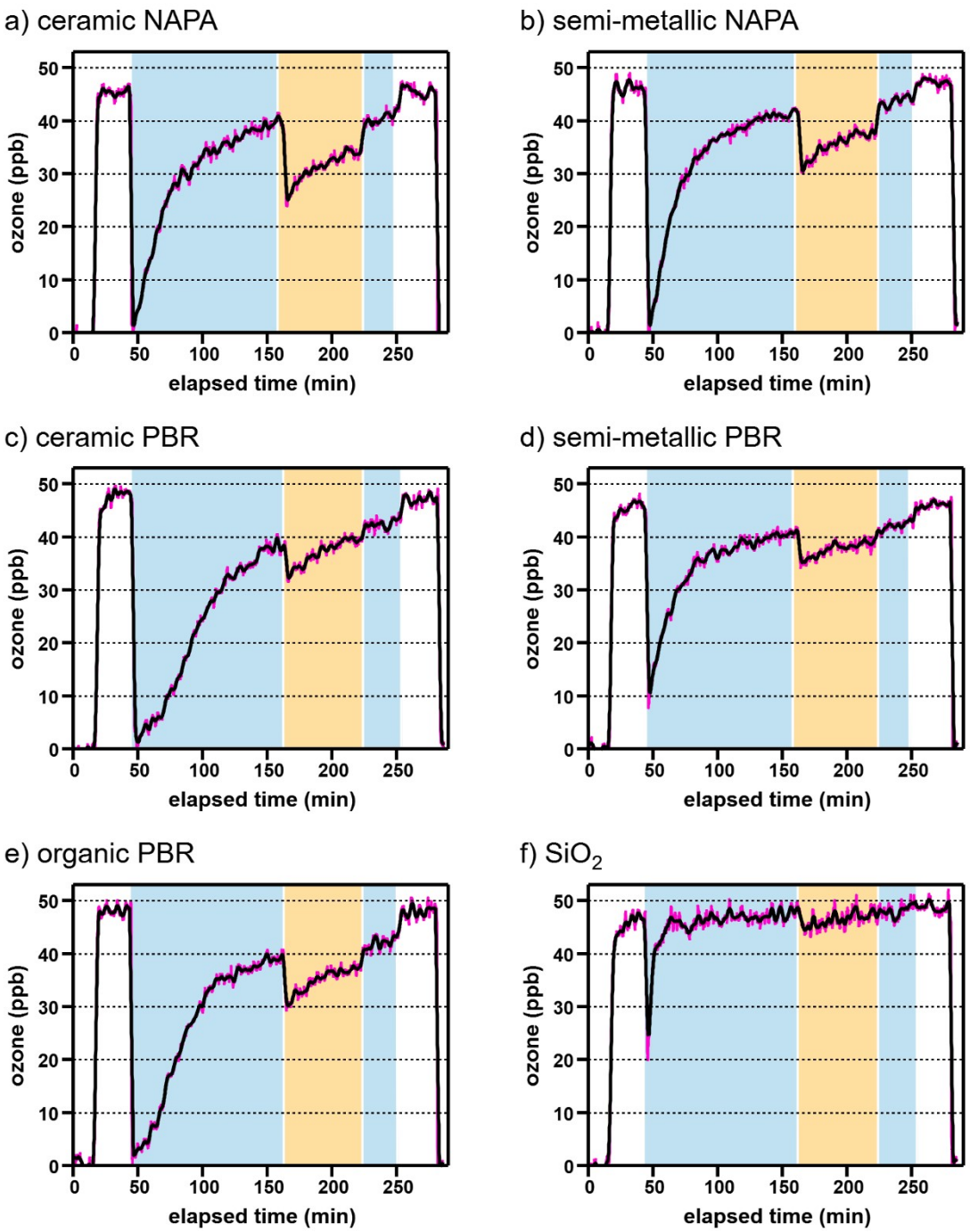

Fig. S2 Representative reaction profiles for the six brake pad components. The blue and yellow underlays indicate periods of exposure to ozone in the dark and light, respectively. The black line is smoothed data (3 min moving average) and the pink line is the original unsmoothed data.

a) phenolic resin

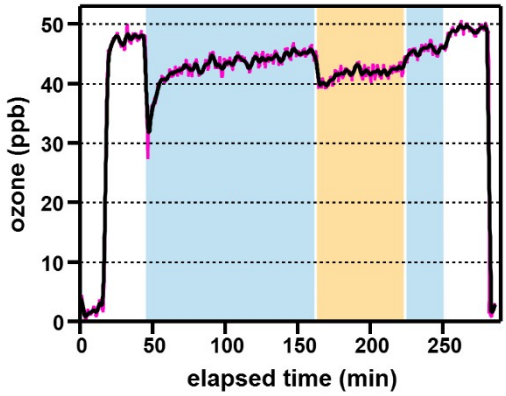

b) graphite

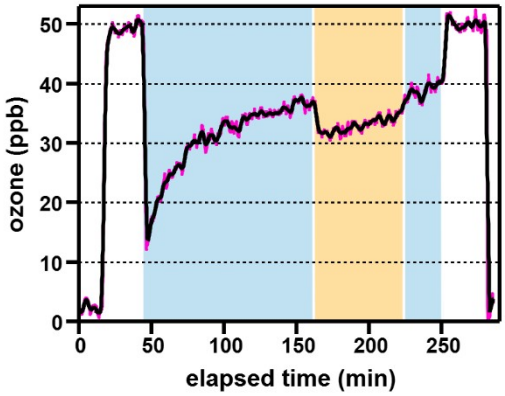

c) Fe_2O_3

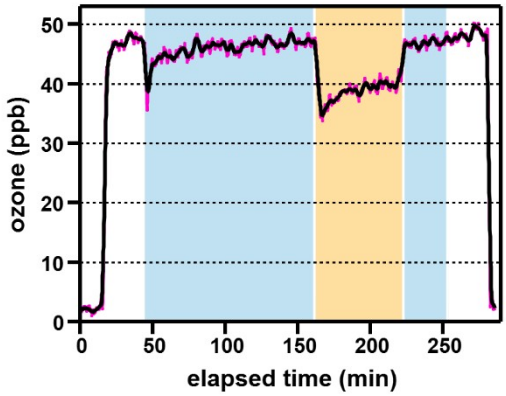

d) Fe_3O_4

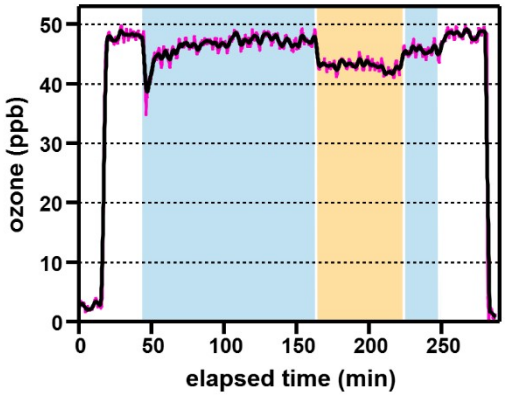

e) Fe powder

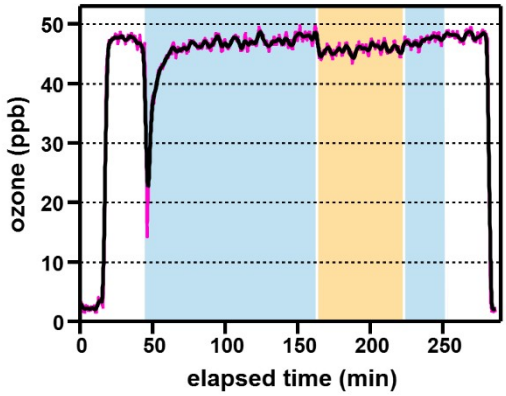

f) Cu powder

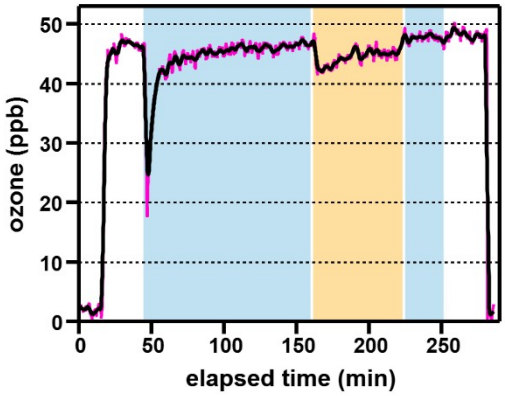

Fig. S3 TGA curves for the five brake pads. The first and second mass losses correspond to oxidative degradation of the organic species and elemental carbon species, respectively. For the semi-metallic PBR sample, determination of organic and elemental carbon content was limited by iron oxidation; for this reason, mass losses are not shown. Further details are presented in **Section S2.3**.

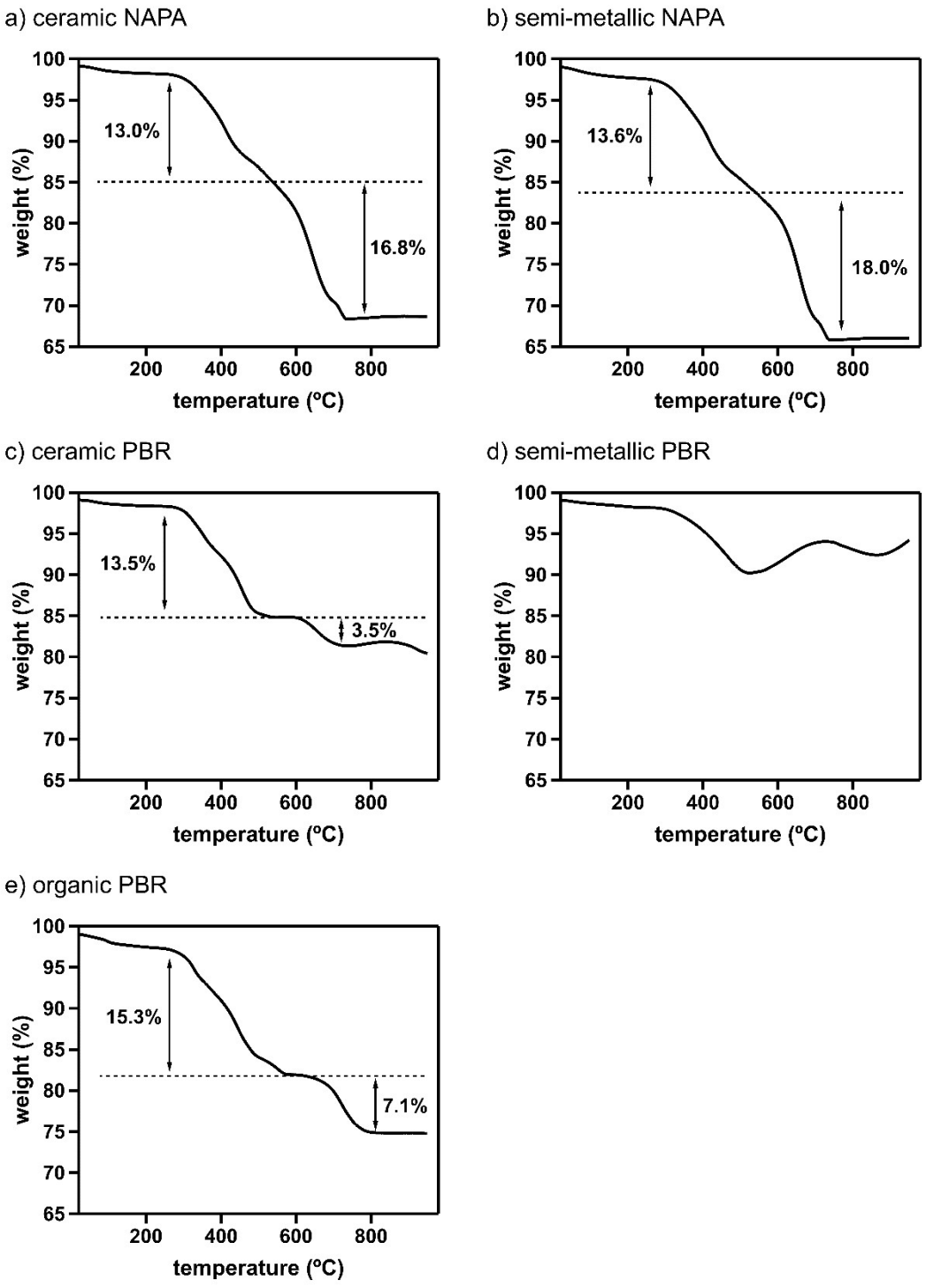

5 Supporting tables

Table S1. Brake pad part numbers and compatible vehicle information (all purchased from www.napacanada.com).

sample name	part number	compatible vehicles
ceramic (NAPA)	FNT PF7574 X	Buick (numerous models, 1997–2005) Cadillac (numerous models, 1997–2005) Chevrolet (numerous models, 1997–2005) Oldsmobile (numerous models, 1997–2004) Pontiac (numerous, models, 1997–2005)
semi-metallic (NAPA)	FNT PF7574 M	
ceramic (PBR)	ALT D1043 C	Infinity FX35 and FX45 (2003–2006) Nissan Altima (2005–2006) Nissan Maxima (2004–2008) Nissan Murano (2003–2007, 2009–2012)
semi-metallic (PBR)	ALT D1043 M	
organic (PBR)	ALT D1043 DP	

Table S2. Mass of sample, mass of SiO_2, and weight percentage of sample used for coated-wall flow tube experiments.

sample	mass sample (mg)	mass SiO_2 (mg)	wt. % sample
ceramic NAPA	1.55 ± 0.07	8.6 ± 0.1	15.3 ± 0.5
semi-metallic NAPA			
organic PBR			
ceramic PBR	2.49 ± 0.05	7.6 ± 0.1	24.7 ± 0.5
semi-metallic PBR			
components	3.6 ± 0.1	6.67 ± 0.08	35.09 ± 0.5

Table S3. BET specific surface areas for all samples; reported errors are calculated as described in **Section S1.9**.

sample	BET surface area ($m^2\ g^{-1}$)
ceramic NAPA	4.45 ± 0.01
semi-metallic NAPA	4.43 ± 0.01
ceramic PBR	2.11 ± 0.02
semi-metallic PBR	2.99 ± 0.01
organic PBR	5.25 ± 0.02
SiO_2	7.57 ± 0.02
phenolic resin	1.75 ± 0.01
graphite	15.35 ± 0.03
Fe_2O_3 (hematite)	8.50 ± 0.02
Fe_3O_4 (magnetite)	7.41 ± 0.01
Fe powder	1.97 ± 0.14
Cu powder	1.26 ± 0.09

Table S4. Elemental composition (wt. %, all elements > 0.1% for at least one sample are shown) of all brake pads, obtained by ICP-MS and total C/N analysis.

element	ceramic NAPA	semi-metallic NAPA	ceramic PBR	semi-metallic PBR	organic PBR
Mg	0.27	0.11	2.85	1.34	0.19
Al	0.98	0.95	0.45	-	0.91
K	0.68	0.56	0.21	-	0.10
Ca	2.93	3.29	0.68	0.13	3.67
Ti	0.36	0.19	-	-	-
Fe	9.38	10.87	33.27	72.84	0.51
Mn	-	-	0.23	-	-
Cu	0.67	0.50	6.58	1.25	7.62
Zn	0.53	0.14	2.37	0.97	-
Mo	-	-	0.22	-	-
Sn	0.34	0.10	-	-	-
Sb	0.10	0.33	3.62	-	1.47
Ba	0.98	0.56	-	1.00	-
C	26.11	26.71	21.56	21.91	20.31
N	0.55	0.54	0.55	0.35	0.55
total	**44.08**	**45.07**	**72.84**	**100.29**	**35.66**

Table S5. Crystalline phases identified by XRD in the brake pads. Diffraction patterns are provided in a separate Supporting Information file (XRD diffraction patterns.pdf).

ceramic NAPA	semi-metallic NAPA	ceramic PBR	semi-metallic PBR	organic PBR
"good" phase matches (see Section S2.1)				
baryte	baryte	iron	iron	baryte
magnetite	magnetite	magnesium copper oxide	baryte	copper zinc *or* silicon copper *or* iron carbon *or* copper
graphite	graphite	graphite	graphite	
illite *or* muscovite	muscovite	zinc cobalt sulfide		5-(4-methoxyphenyl)tetrazole
	wüstite			
	potassium zinc silicate			
"potential" phase matches (see Section S2.1)				
wüstite	zircon	zircon	zircon	
titanium carbide		clinochlore	silicon oxide	
zinc sulfide		copper		
calcium magnesium sulfide		copper manganese oxide		
copper zinc oxide		copper manganese antimony oxide		
silicon oxide		cobalt iron cyanide hydrate		
		molybdenum tin zirconium		
		copper molybdenum		
		copper nickel manganese oxide *or* lithium manganese oxide		

Table S6. List of components present in the NAPA brake pads obtained from the safety data sheets (SDS),[30] which reported components present at > 1 wt. %.

ceramic NAPA	semi-metallic NAPA
phenolic resin	phenolic resin
aramid pulp	aramid pulp
cashew resin – cured	cashew resin – cured
graphite	graphite
iron oxide	iron oxide
barium sulfate	barium sulfate
potassium titanate	aluminum oxide
brass chips	steel fibers
mineral fibers	carbon black

Table S7. List of possible components present in the brake pads for all elements detected using ICP-MS and combustion analysis, based on available literature.[12,15,17,22] This list represents components that may be present in the samples, but were not identified by XRD, and is not necessarily an exhaustive list.

element	possible component assignment
Mg	magnesium oxide (MgO), clays (*e.g.*, mica)
Al	aluminum oxide (Al_2O_3), clays (*e.g.*, mica)
K	potassium titanate, clays (*e.g.*, mica)
Ca	calcium carbonate ($CaCO_3$), calcium oxide (CaO), clays (*e.g.*, mica)
Ti	potassium titanate (K_2TiO_3)
Mn	clays (*e.g.*, mica)
Fe	iron oxides (*e.g.,* Fe_2O_3 and Fe_3O_4), steel fibers, iron chips
Cu	copper powder, brass chips, copper sulfide (CuS)
Zn	zinc sulfide (ZnS), brass chips
Mo	molybdenum disulfide (MoS_2), molybdenum trioxide (MoO_3)
Sn	tin sulfide (SnS)
Sb	antimony trisulfide (Sb_2S_3), antimony sulfate ($Sb_2(SO_4)_3$)
Ba	barium sulfate ($BaSO_4$)
C	phenolic resin, aramid fibers, cashew resin, graphite, carbon black
N	aramid fibers

Table S8. Steady-state ozone uptake coefficients ($\gamma_{BET,SS}$) for brake pads and brake pad components. Reported uncertainties were obtained from error propagation, as described in **Section S1.10**.

sample	$\gamma_{BET,SS}$ dark ($\times 10^{-6}$)	$\gamma_{BET,SS}$ light ($\times 10^{-6}$)
ceramic NAPA	1.6 ± 0.5	4.6 ± 0.5
	1.7 ± 0.6	4.3 ± 0.8
	1.2 ± 0.4	2.9 ± 0.5
semi-metallic NAPA	1.4 ± 0.4	3.9 ± 0.5
	1.4 ± 0.4	3.8 ± 0.5
	0.9 ± 0.4	3.3 ± 0.5
ceramic PBR	2.7 ± 0.5	4.2 ± 0.5
	2.5 ± 0.6	4.8 ± 0.7
	3.9 ± 0.9	6.0 ± 0.7
semi-metallic PBR	1.9 ± 0.3	2.7 ± 0.5
	1.1 ± 0.4	2.0 ± 0.5
	1.2 ± 0.3	2.6 ± 0.5
organic PBR	2.1 ± 0.5	4.0 ± 0.5
	2.0 ± 0.5	3.9 ± 0.7
	1.9 ± 0.5	4.9 ± 0.5
phenolic resin	1.8 ± 0.7	2.9 ± 0.6
	1.9 ± 0.4	3.2 ± 0.4
graphite	0.63 ± 0.08	1.0 ± 0.1
	0.57 ± 0.06	0.81 ± 0.09
Fe powder	0.2 ± 0.8 **	0.8 ± 0.8 **
	1.9 ± 1.6	0.5 ± 0.4
Fe_2O_3	0.02 ± 0.09 **	0.38 ± 0.09
	0.11 ± 0.05	0.64 ± 0.08
Fe_3O_4	0.22 ± 0.07	0.3 ± 0.1
	0.3 ± 0.1	0.6 ± 0.1
Cu powder	0.3 ± 0.5 **	1.8 ± 0.7
	N/A *	1.4 ± 1.2

* For one Cu powder trial, $k_{obs,total}$ was smaller than k_{obs,SiO_2}, which resulted in a negative $k_{obs,sample}$; thus, $\gamma_{BET,SS,\,dark}$ is not reported.

** For these trials, we note that ranges encompass zero, which reflects the similarity of $k_{obs,total}$ to k_{obs,SiO_2} (*i.e.*, the low ozone uptake by the samples at the masses employed here).

Table S9. Time-dependent ozone uptake coefficients ($\gamma_{BET,15min}$, $\gamma_{BET,30min}$, and $\gamma_{BET,60min}$) for brake pads and brake pad components. Reported uncertainties were obtained from error propagation, as described in **Section S1.10**. Due to their high diffusion correction factors (see **Section S1.7**), $\gamma_{BET,15min}$ for the brake pads are not reported.

sample	$\gamma_{BET,\ 15min}$ ($\times 10^{-6}$)	$\gamma_{BET,\ 30min}$ ($\times 10^{-6}$)	$\gamma_{BET,\ 60min}$ ($\times 10^{-6}$)
ceramic NAPA	–	9.6 ± 0.5	4.3 ± 0.5
	–	13.0 ± 0.9	4.4 ± 0.7
	–	7.9 ± 0.6	3.0 ± 0.6
semi-metallic NAPA	–	12.8 ± 0.8	4.7 ± 0.6
	–	7.9 ± 0.7	3.7 ± 0.5
	–	8.7 ± 0.7	3.5 ± 0.5
ceramic PBR	–	61 ± 2	18 ± 1
	–	89 ± 4	23 ± 1
	–	108 ± 7	27 ± 1
semi-metallic PBR	–	9.3 ± 0.4	3.6 ± 0.4
	–	5.6 ± 0.6	2.5 ± 0.4
	–	7.0 ± 0.4	3.2 ± 0.4
organic PBR	–	24.2 ± 0.8	6.1 ± 0.5
	–	36 ± 1	8.3 ± 0.6
	–	31 ± 1	11.2 ± 0.7
phenolic resin	5.0 ± 0.7	3.9 ± 0.6	3.0 ± 0.6
	3.5 ± 0.5	2.9 ± 0.4	2.5 ± 0.4
graphite	2.5 ± 0.2	1.57 ± 0.09	1.2 ± 0.1
	4.7 ± 0.2	2.53 ± 0.09	1.50 ± 0.07
Fe powder	N/A *	1 ± 1 **	0.5 ± 1 **
	0.8 ± 0.4	0.5 ± 0.4	0.4 ± 0.4 **
Fe_2O_3	0.05 ± 0.09 **	0.0007 ± 0.09 **	0.01 ± 0.09 **
	0.1 ± 0.1 **	0.21 ± 0.07	0.02 ± 0.07 **
Fe_3O_4	0.11 ± 0.09	0.09 ± 0.08	0.17 ± 0.08
	0.13 ± 0.09	0.11 ± 0.08	0.02 ± 0.08 **
Cu powder	4.7 ± 0.8	2.4 ± 0.7	1.6 ± 0.7
	2.7 ± 0.9	0.7 ± 0.9 **	N/A *

* For some trials, $k_{obs,total}$ was smaller than k_{obs,SiO_2}, which resulted in a negative $k_{obs,sample}$; thus, $\gamma_{BET,SS,\ dark}$ are not reported.

** For these trials, we note that ranges encompass zero, which reflects the similarity of $k_{obs,total}$ to k_{obs,SiO_2} (*i.e.*, the low ozone uptake by the samples at the masses employed here).

Table S10. Average uptake coefficient diffusion correction factors ($(\gamma_{corr}/\gamma_{eff} - 1) \times 100$) for the brake pads and brake pad components as calculated in **Section S1.7**. The brake pad $\gamma_{BET,15min}$ correction factors were very high (see **Section S1.7**), so both $\gamma_{BET,15min}$ and its correction factors are not reported.

sample	15 min (%)	30 min (%)	60 min (%)	dark steady-state (%)	light steady-state (%)
ceramic NAPA	–	23	9	3	10
semi-metallic NAPA	–	69	10	3	9
ceramic PBR	–	117	31	4	8
semi-metallic PBR	–	16	7	3	6
organic PBR	–	73	21	5	11
phenolic resin	8	6	5	3	5
graphite	52	30	20	8	14
Fe powder	3	2	1	< 1	2
Fe_2O_3	3	2	1	< 1	6
Fe_3O_4	3	2	2	2	4
Cu powder	4	2	1	< 1	2

Table S11. Average ratios of time-dependent to steady-state uptake coefficients ($\gamma_{BET,t}$ / $\gamma_{BET,SS}$) for brake pads (n = 3) and brake pad components (n = 2). We did not report $\gamma_{BET,15min}$ for brake pads, as diffusion correction factors are excessively high (see **Section S1.7**).

sample	$\gamma_{BET,15min}$ / $\gamma_{BET,SS}$	$\gamma_{BET,30min}$ / $\gamma_{BET,SS}$	$\gamma_{BET,60min}$ / $\gamma_{BET,SS}$
ceramic NAPA	–	7	3
semi-metallic NAPA	–	8	3
ceramic PBR	–	29	8
semi-metallic PBR	–	5	2
organic PBR	–	15	4
phenolic resin	3	2	2
graphite	6	3	2
Fe powder	4 and N/A*	4	2
Fe_2O_3	2	1	0.6
Fe_3O_4	0.5	0.4	0.5
Cu powder	17 and N/A*	8 and N/A*	6 and N/A*

*Ratios could not be calculated in cases where $k_{obs,total}$ was smaller than k_{obs,SiO_2}, as this resulted in an apparent "negative" γ_{BET}.

6 References

(1) M. Abou-Ghanem, A. O. Oliynyk, Z. Chen, L. C. Matchett, D. T. McGrath, J. M. Katz, A. J. Locock and S. A. Styler, Significant variability in the photocatalytic activity of natural titanium-containing minerals: Implications for understanding and predicting atmospheric mineral dust photochemistry, *Environ. Sci. Technol.,* 2020, **54**, 13509–13516.

(2) D. D. Parrish, P. C. Murphy, D. L. Albritton and F. C. Fehsenfeld, The measurement of the photodissociation rate of NO_2 in the atmosphere, *Atmos. Environ.,* 1983, **17**, 1365–1379.

(3) L. Zafonte, P. L. Rieger and J. R. Holmes, Nitrogen dioxide photolysis in the Los Angeles atmosphere, *Environ. Sci. Technol.,* 1977, **11**, 483–487.

(4) C. E. Kolb, R. A. Cox, J. P. D. Abbatt, M. Ammann, E. J. Davis, D. J. Donaldson, B. C. Garrett, C. George, T. Griffiths, D. R. Hanson, M. Kulmala, G. McFiggans, U. Poschl, I. Riipinen, M. J. Rossi, Y. Rudich, P. M. Winkler, D. R. Worsnop and C. D. O' Dowd, An overview of current issues in the uptake of atmospheric trace gases by aerosols and clouds, *Atmos. Chem. Phys.*, 2010, **10**, 10561–10605.

(5) U. Pöschl, Y. Rudich and M. Ammann, Kinetic model framework for aerosol and cloud surface chemistry and gas-particle interactions – Part 1: General equations, parameters, and terminology, *Atmos Chem Phys,* 2007, **7**, 5989–6023.

(6) D. A. Knopf, U. Pöschl and M. Shiraiwa, Radial diffusion and penetration of gas molecules and aerosol particles through laminar flow reactors, denuders, and sampling tubes, *Anal. Chem.,* 2015, **87**, 3746–3754.

(7) Z. L. Coates Fuentes, T. M. Kucinski and R. Z. Hinrichs, Ozone decomposition on kaolinite as a function of monoterpene exposure and relative humidity, *ACS Earth Space Chem.,* 2018, **2**, 21–30.

(8) M. Nicolas, M. Ndour, O. Ka, B. D'Anna and C. George, Photochemistry of atmospheric dust: Ozone decomposition on illuminated titanium dioxide, *Environ. Sci. Technol.,* 2009, **43**, 7437–7442.

(9) D. A. Gómez-Gualdrón, P. Z. Moghadam, J. T. Hupp, O. K. Farha and R. Q. Snurr, Application of consistency criteria to calculate BET areas of micro- and mesoporous metal–organic frameworks, *J. Am. Chem. Soc.,* 2016, **138**, 215–224.

(10) J. H. J. Hulskotte, G. D. Roskam and H. A. C. Denier van der Gon, Elemental composition of current automotive braking materials and derived air emission factors, *Atmos. Environ.*, 2014, **99**, 436–445.

(11) J. Wahlström, L. Olander and U. Olofsson, Size, shape, and elemental composition of airborne wear particles from disc brake materials, *Tribol. Lett.*, 2010, **38**, 15–24.

(12) J. Kukutschová, P. Moravec, V. Tomášek, V. Matějka, J. Smolík, J. Schwarz, J. Seidlerová, K. Šafářová and P. Filip, On airborne nano/micro-sized wear particles released from low-metallic automotive brakes, *Environ. Pollut.*, 2011, **159**, 998–1006.

(13) M. Alemani, O. Nosko, I. Metinoz and U. Olofsson, A study on emission of airborne wear particles from car brake friction pairs, *SAE Int. J. Mater. Manuf.*, 2016, **9**, 147–157.

(14) P. C. Verma, M. Alemani, S. Gialanella, L. Lutterotti, U. Olofsson and G. Straffelini, Wear debris from brake system materials: A multi-analytical characterization approach, *Tribol. Int.*, 2016, **94**, 249–259.

(15) D. Chan and G. W. Stachowiak, Review of automotive brake friction materials, *Proc. Inst. Mech. Eng. Part D*, 2004, **218**, 953–966.

(16) P. G. Sanders, N. Xu, T. M. Dalka and M. M. Maricq, Airborne brake wear debris: Size distributions, composition, and a comparison of dynamometer and vehicle tests, *Environ. Sci. Technol.*, 2003, **37**, 4060–4069.

(17) J. Kukutschová, V. Roubíček, M. Mašláň, D. Jančík, V. Slovák, K. Malachová, Z. Pavlíčková and P. Filip, Wear performance and wear debris of semimetallic automotive brake materials, *Wear*, 2010, **268**, 86–93.

(18) S. Ramousse, J. W. Hoj and O. T. Sorensen, Thermal characterisation of brake pads, *J. Therm. Anal. Calorim.*, 2001, **64**, 933–943.

(19) M. Li, H. Su, G. Li, N. Ma, U. Pöschl and Y. Cheng, Relative importance of gas uptake on aerosol and ground surfaces characterized by equivalent uptake coefficients, *Atmospheric Chem. Phys.*, 2019, **19**, 10981–11011.

(20) C.-H. Jeong, J. M. Wang, N. Hilker, J. Debosz, U. Sofowote, Y. Su, M. Noble, R. M. Healy, T. Munoz, E. Dabek-Zlotorzynska, V. Celo, L. White, C. Audette, D. Herod and G. J. Evans, Temporal and spatial variability of traffic-related PM2.5 sources: Comparison of exhaust and non-exhaust emissions, *Atmos. Environ.*, 2019, **198**, 55–69.

(21) F. Amato, M. Pandolfi, A. Escrig, X. Querol, A. Alastuey, J. Pey, N. Perez and P. K. Hopke, Quantifying road dust resuspension in urban environment by Multilinear Engine: A comparison with PMF2, *Atmos. Environ.*, 2009, **43**, 2770–2780.

(22) T. Grigoratos and G. Martini, Brake wear particle emissions: a review, *Environ. Sci. Pollut. Res.*, 2015, **22**, 2491–2504.

(23) P. Herckes, G. Engling, S. M. Kreidenweis and J. L. Collett, Particle size distributions of organic aerosol constituents during the 2002 Yosemite Aerosol Characterization Study, *Environ. Sci. Technol.*, 2006, **40**, 4554–4562.

(24) S. Nakao, P. Tang, X. Tang, C. H. Clark, L. Qi, E. Seo, A. Asa-Awuku and D. Cocker, Density and elemental ratios of secondary organic aerosol: Application of a density prediction method, *Atmos. Environ.*, 2013, **68**, 273–277.

(25) M. S. Alam, S. Zeraati-Rezaei, H. Xu and R. M. Harrison, Characterization of gas and particulate phase organic emissions (C_9 –C_{37}) from a diesel engine and the effect of abatement devices, *Environ. Sci. Technol.*, 2019, **53**, 11345–11352.

(26) D. R. Worton, G. Isaacman, D. R. Gentner, T. R. Dallmann, A. W. H. Chan, C. Ruehl, T. W. Kirchstetter, K. R. Wilson, R. A. Harley and A. H. Goldstein, Lubricating oil dominates primary organic aerosol emissions from motor vehicles, *Environ. Sci. Technol.*, 2014, **48**, 3698–3706.

(27) B. D'Anna, A. Jammoul, C. George, K. Stemmler, S. Fahrni, M. Ammann and A. Wisthaler, Light-induced ozone depletion by humic acid films and submicron aerosol particles, *J. Geophys. Res.*, 2009, **114**, D12301.

(28) D. A. Knopf, L. M. Anthony and A. K. Bertram, Reactive uptake of O_3 by multicomponent and multiphase mixtures containing oleic acid, *J. Phys. Chem. A*, 2005, **109**, 5579–5589.

(29) T. Moise and Y. Rudich, Reactive uptake of ozone by proxies for organic aerosols: Surface versus bulk processes, *J. Geophys. Res. Atmospheres*, 2000, **105**, 14667–14676.

(30) Personal communication with a NAPA Canada representative. Safety Data Sheets PF7574X and PF7574M; Aug 29, 2018.